Nuclear Science and Techniques (2025) 36:216
https://doi.org/10.1007/s41365-025-01795-0

The dynamical mechanism in the fusion reactions to synthesize neutron-deficient Pu isotopes

Zi-Long Wang[1] · Xiao-Ye Zhang[1] · Gen Zhang[1] · Feng-Shou Zhang[2,3,4]

Received: 20 December 2024 / Revised: 31 March 2025 / Accepted: 20 April 2025 / Published online: 30 August 2025

Abstract
Within the framework of the isospin-dependent quantum molecular dynamics model, the fusion cross section and fusion mechanism of neutron-deficient Pu isotopes in the reactions ^{24,26,30}Si+^{196}Hg were investigated. We found that the fusion cross sections are higher in the reaction with a more neutron-rich beam owing to the lower dynamical barrier. The dynamical barrier decreases with decreasing incident energy, which explains the fusion enhancement at the sub-barrier energy. The peak value of *N*/*Z* ratio in the neck region is the highest in reaction ^{30}Si+^{196}Hg, indirectly leading to the lowest dynamical barrier. Compared with the proton density distribution, the neck region for neutrons is larger, indicating that neutrons transfer more quickly than protons, leading to a high *N*/*Z* ratio in the neck. The time distribution of the appearance of dynamical barriers is wider at lower incident energies, indicating that the fusion process took longer to exchange nucleons. The single-particle potential barrier decreases with time evolution and finally disappears at a lower impact parameter, which is favorable for fusion events.

Keywords Fusion reaction · Neutron-deficient isotopes · Neck dynamics · IQMD model

1 Introduction

The synthesis of new nuclides has always been a hot topic in the field of nuclear physics and is essential for exploring the existence limits of nuclei, exotic nuclear structures, and nuclear forces. According to theoretical predictions, a large number of nuclides are yet to be discovered [1], especially in superheavy and neutron-rich regions. However, there is still a blank area on the neutron-deficient side with $Z > 82$. To date, the different methods used to produce unknown nuclei include nuclear fission, projectile fragmentation, fusion evaporation, and light particle reactions [2, 3], which are applicable across different regions of the nuclear chart. Most neutron-deficient nuclei are synthesized via fusion–evaporation reactions. The study of heavy-ion fusion reactions at energies near the Coulomb barrier, involving nuclear structure effects, barrier distribution, and nucleon transfer, is beneficial for exploring the synthesis mechanism of neutron-deficient nuclei [4–7] and to provide the optimal projectile–target combinations for the experiments.

The synthesis of neutron-deficient nuclei is crucial for the investigation of proton halos, emergence of new magic numbers, β-delayed fission, proton decay mode, and shape evolution [8–13]. The Pu isotopes are in the actinide region, and some neutron-deficient Pu isotopes have not yet been discovered. Currently, 21 Pu isotopes have been experimentally synthesized. The earliest experiment can be traced back to 1946 at the Lawrence Berkeley National Laboratory (LBNL) [14], where the target ^{238}U was irradiated with neutrons and ^{239}Pu was produced by successive β decays. Over the next

This work was supported by the National Natural Science Foundation of China (No. 12405145).

✉ Gen Zhang
zhanggen@gxu.edu.cn

[1] Guangxi Key Laboratory for Relativistic Astrophysics, School of Physical Science and Technology, Guangxi University, Nanning 530004, China

[2] The Key Laboratory of Beam Technology of Ministry of Education, School of Physics and Astronomy, Beijing Normal University, Beijing 100875, China

[3] Institute of Radiation Technology, Beijing Academy of Science and Technology, Beijing 100875, China

[4] National Laboratory of Heavy Ion Accelerator of Lanzhou, Center of Theoretical Nuclear Physics, Lanzhou 730000, China

30 years, LBNL continued to accelerate light particles, such as ^{3,4}He and ^{2}H, bombarding the U target, and $^{231\text{-}241}$Pu were successively produced [15–21]. In addition, for the neutron-deficient region, ^{207,208}Pb target was impinged by ^{24,26}Mg beam in the laboratory at JINR, the isotopes $^{228\text{-}230}$Pu were generated in the 4n and 5n evaporation channels [22, 23], and ^{227}Pu was produced in the reaction ^{192}Os(^{40}Ar, 5n)^{227}Pu at the Institute of Modern Physics [24]. In the neutron-rich region, $^{242\text{-}245}$Pu and ^{247}Pu isotopes were produced by neutron capture reactions on actinides targets [25–29]. The isotope ^{246}Pu was detected in the debris from the thermonuclear test [30]. The fusion–evaporation reaction is more suitable and promising for the synthesis of more neutron-deficient unknown Pu isotopes.

Over the past few decades, various models have been developed to describe the fusion reactions. Macroscopic models can describe the evolution of multiple degrees of freedom, including charge and mass asymmetry, elongation of a mononucleus, and surface deformations, such as the dinuclear system (DNS) model [31–36], Langevin equations [37–39], two-step model [40], fusion by diffusion (FBD) model [41, 42], empirical model [43, 44], and dynamical cluster-decay model [45, 46]. For self-consistent consideration of the dynamical effects, the time-dependent Hartree–Fock (TDHF) model [47–49], as a microscopic quantum transport theory based on the mean field, can reasonably predict the fusion cross sections. The isospin-dependent quantum molecular dynamics (IQMD) model [6, 50], as a semi-classical microscopic dynamics transport model that includes two-body collision and phase-space constraint, has been successful in investigating neck dynamics and fusion mechanisms.

The remainder of this paper is organized as follows. In Sect. 2, the framework of the IQMD model is introduced. In Sect. 3, the calculated results and discussion are presented. Finally, a summary is presented in Sect. 4.

2 The model

Based on the conventional QMD model, the interaction potential, nucleon's fermionic nature, and two-body collision were improved in the IQMD. In this model, the nucleon i is described by a coherent state of a Gaussian wave packet,

$$\psi_i(\mathbf{r},t)=\frac{1}{(2\pi L)^{3/4}}\exp\left[-\frac{(\mathbf{r}-\mathbf{r}_i(t))^2}{4L}+\frac{i\mathbf{p}_i(t)\cdot\mathbf{r}}{\hbar}\right]. \tag{1}$$

Here, $L=\sigma_r^2$, and σ_r denotes the width of the wave packet in the coordinate space, calculated as $0.09A^{1/3}$+0.88, in which A is the mass number of the nucleus. $\mathbf{r}_i$ and $\mathbf{p}_i$ represent the centers of the ith wave packet in the coordinate and momentum space, respectively.

The phase-space density distribution of nucleon i can be derived from the wave function through the Wigner transformation, expressed as

$$\begin{aligned} f_i(\mathbf{r},\mathbf{p},t)=&\frac{1}{(\pi\hbar)^3}\exp\left[-\frac{(\mathbf{r}-\mathbf{r}_i(t))^2}{2L}\right]\\ &\times\exp\left[-\frac{(\mathbf{p}-\mathbf{p}_i(t))^2\cdot 2L}{\hbar^2}\right]. \end{aligned} \tag{2}$$

Using the generalized variational principle, the motion equation of each nucleon can be derived as follows:

$$\dot{\mathbf{r}}_i=\frac{\partial\langle H\rangle}{\partial\mathbf{p}_i}, \tag{3}$$

$$\dot{\mathbf{p}}_i=-\frac{\partial\langle H\rangle}{\partial\mathbf{r}_i}. \tag{4}$$

Here, H denotes the Hamiltonian of the system, expressed as

$$H=\int\epsilon_{\rm loc}[\rho(\mathbf{r})]d\mathbf{r}+U_{\rm Coul}+T, \tag{5}$$

where $U_{\rm Coul}$ and T represent the Coulomb potential and the kinetic energy, respectively. The local energy density functional $\epsilon_{\rm loc}$ is derived from Skyrme interaction without the spin-orbit term [51, 52] and consists of two-body term, three-body term, surface term, symmetry term, and effective mass term, shown as

$$\begin{aligned} \epsilon_{\rm loc}(\rho(\mathbf{r}))=&\frac{\alpha}{2}\frac{\rho(\mathbf{r})^2}{\rho_0}+\frac{\beta}{\gamma+1}\frac{\rho(\mathbf{r})^{\gamma+1}}{\rho_0^{\gamma}}+\frac{g_{\rm sur}}{2\rho_0}\nabla^2\rho(\mathbf{r})\\ &+\frac{C_{\rm sym}}{2\rho_0}\left[\rho(\mathbf{r})^2-k_{\rm s}\nabla^2\rho(\mathbf{r})\right]\delta^2+g_\tau\frac{\rho(\mathbf{r})^{\eta+1}}{\rho_0^{\eta}}, \end{aligned} \tag{6}$$

where

$$\rho(\mathbf{r})=\sum_i\frac{1}{(2\pi L)^{3/2}}\exp\left[-\frac{(\mathbf{r}-\mathbf{r}_i(t))^2}{2L}\right]. \tag{7}$$

Here, $\rho(\mathbf{r})$ represents the density distribution in the coordinate space, which is derived from the phase-space density distribution by integrating over the full momentum space. $\delta=(\rho_{\rm n}-\rho_{\rm p})/(\rho_{\rm n}+\rho_{\rm p})$ represents isospin asymmetry, where $\rho_{\rm n}$ and $\rho_{\rm p}$ denote the density distributions of neutrons and protons, respectively. The corresponding model parameters [53] are listed in Table 1. In Fig. 1, the time evolution of root-mean-square radii and binding energies of ^{30}Si and ^{196}Hg are shown. It can be found that those physical variables can remain stable for a long time, indicating the functional can describe the basic nuclear properties well.

The long-range Coulomb potential is also a function of the density distribution:

Table 1 The model parameters (IQ2) adopted in this work

α (MeV)	β (MeV)	γ	$g_{\rm sur}$ (MeV·fm^2)	g_τ (MeV)	η	$C_{\rm sym}$ (MeV)	$\kappa_{\rm s}$(fm^2)	ρ_0(fm^{-3})
− 356	303	7/6	7.0	12.5	2/3	32	0.08	0.165

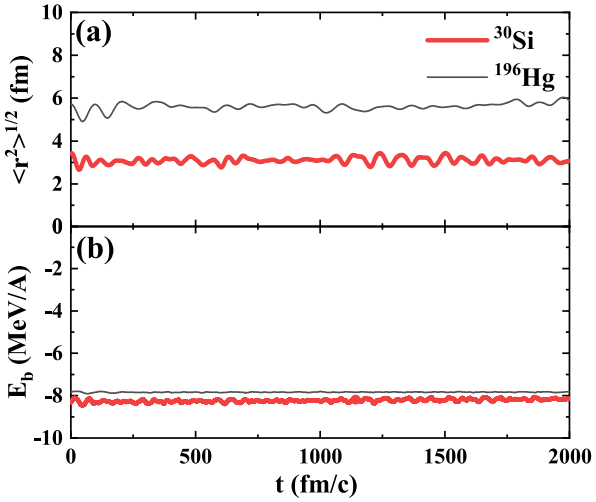

Fig. 1 The time evolution of root-mean-square radii (**a**) and binding energies (**b**) of ^{30}Si and ^{196}Hg, represented by thick and thin lines, respectively

$$U_{\rm Coul} = \frac{1}{2}\sum_{\substack{i\neq j\\(i,j\in\text{proton})}}\int \rho_i(\mathbf{r})\frac{e^2}{|\mathbf{r}-\mathbf{r}'|}\rho_j(\mathbf{r}')\mathrm{d}\mathbf{r}\mathrm{d}\mathbf{r}' - e^2\frac{3}{4}\left(\frac{3}{\pi}\right)^{1/3}\int \rho_{\rm p}(\mathbf{r})^{4/3}\mathrm{d}\mathbf{r}, \tag{8}$$

where the second term represents the Coulomb exchange potential.

The kinetic energy of the system is calculated by

$$T = \sum_i\left(\frac{p_i^2}{2m} + \frac{3\hbar^2}{8mL}\right), \tag{9}$$

where the second term arises from the diffusion of Gaussian wave packets in momentum space, and m is the mass of the nucleon.

The wave function of the system is adopted as the direct product of the single-particle wave functions as follows:

$$\phi(\mathbf{r},t) = \prod_i \psi_i(\mathbf{r},t). \tag{10}$$

Therefore, the wave function does not satisfy the demand for anti-symmetrization. To compensate for the fermionic property, a phase-space occupancy constraint method was proposed [54]. The occupancy rate of the nucleon i is defined as follows:

$$\bar{f}_i = \sum_j \delta_{s_i s_j}\delta_{\tau_i\tau_j}\int_{h^3} f_j(\mathbf{r},\mathbf{p},t)\mathrm{d}\mathbf{r}\mathrm{d}\mathbf{p}, \tag{11}$$

where s_i and τ_i are the spin and isospin quantum numbers, respectively. Integration is performed on the phase-space grid around the center of the i-th wave packet, and h^3 is the phase-space volume.

If $\bar{f}_i > 1$, elastic scattering will be conducted to decrease the phase-space occupancy.

To compensate for the short-range repulsion effect of the nuclear force, two nucleons satisfying the following kinematic conditions are scattered:

$$\left|\frac{\Delta\mathbf{r}\cdot\mathbf{p}}{p}\right| \le \left(\frac{p}{\sqrt{p^2+m_1^2}} + \frac{p}{\sqrt{p^2+m_2^2}}\right)\frac{\delta t}{2}, \tag{12}$$

$$\sqrt{(\Delta\mathbf{r})^2 - (\Delta\mathbf{r}\cdot\mathbf{p}/p)^2} \le \sqrt{\sigma_{\rm nn}/\pi}, \tag{13}$$

where $\mathbf{p}$, p, and $\Delta\mathbf{r}$ represent the momentum, magnitude of the momentum, and distance between two nucleons in their center-of-mass system, respectively. The time interval of dynamical evolution δt is taken as 1 fm/c, and $m_{1,2}$ denotes the mass of the nucleon. $\sigma_{\rm nn}$ is the nucleon–nucleon scattering cross section extracted from experiments [55]. The final state is checked to determine whether this scattering is allowed according to the Pauli blocking.

To establish the initial conditions of the system, the Skyrme–Hartree–Fock method was applied to provide the density distribution of protons and neutrons in both the projectile and the target nuclei. Subsequently, the Monte Carlo method was employed to sample the coordinates and momenta of nucleons. The sampling range of the momentum was from zero to the Fermi momentum.

The stability of a nucleus is checked by undergoing time evolution over 2000 fm/c within its self-consistent mean field. At each time step, the root-mean-square radius and binding energy of the nucleus were compared with the experimental values.

The fusion cross section is calculated as follows:

$$\sigma_{\rm fus} = 2\pi\sum_b P_{\rm fus} b\Delta b, \tag{14}$$

where $P_{\rm fus}$ represents the fusion probability calculated as the ratio of the number of fusion events to the total number of events. b denotes the impact parameter and Δb is taken as 1

fm. We simulate 500 events for each impact parameter. In each event, the projectile and target rotated randomly around their respective centers at the initial time to eliminate the influence of the directional effect.

To judge the fusion event, the event is regarded as a fusion event when the distance between two nuclei is less than 3 fm and the mass of the largest cluster formed is close to the mass of the compound nucleus. As for the determination of a cluster, if the relative distance between two nucleons is less than 3 fm, and the relative momentum is less than 0.25 GeV/c, these nucleons are considered as a cluster.

The interaction potential between the projectile and target is calculated by subtracting the energies of the target and projectile from the total energy of the system, which is expressed as

$$V(\mathbf{R}) = \int \epsilon[\rho_{\mathrm{p}}(\mathbf{r}) + \rho_{\mathrm{t}}(\mathbf{r}-\mathbf{R})]\mathrm{d}\mathbf{r} - \int \epsilon[\rho_{\mathrm{p}}(\mathbf{r})]\mathrm{d}\mathbf{r} - \int \epsilon[\rho_{\mathrm{t}}(\mathbf{r}-\mathbf{R})]\mathrm{d}\mathbf{r}, \tag{15}$$

where $\mathbf{R}$ denotes the distance between the centroids of the two nuclei. ρ_{p} and ρ_{t} indicate the density distributions of the projectile and the target, respectively. For the static interaction potential, the density distributions of the projectile and target remained unchanged.

3 Results and discussion

To verify the validity of the IQMD model for describing the fusion reactions, the fusion cross sections were calculated in the reactions of ^{208}Pb+^{26}Mg, ^{28}Si+^{208}Pb, ^{31}Al+^{197}Au, and ^{28}Si+^{198}Pt, as shown in Fig. 2. All compound nuclei in these reactions were around $Z = 94$. The calculated results show a satisfactory agreement with the experimental data [56–59] for both the sub-barrier and above-barrier energies. Within a certain energy range, the corresponding fusion cross section increases with increasing incident energy. The fusion cross sections at a low energy in ^{208}Pb+^{26}Mg reaction are larger than those in ^{28}Si+^{208}Pb, due to the stronger Coulomb repulsion in the latter reaction. Similarly, ^{31}Al+^{197}Au reaction has greater fusion cross sections than those in ^{28}Si+^{198}Pt. These results indicate that Coulomb repulsion plays a substantial role in fusion reactions.

In the following work, systems of ^{24,26,30}Si+^{196}Hg were chosen to investigate the isospin effect on the fusion reaction. In Fig. 3, the fusion cross sections and corresponding static interaction potentials in the three reactions are illustrated. Notably, the fusion cross section in the reaction with a more neutron-rich beam is larger. To explain this phenomenon, we can analyze it in terms of interaction potential. A sudden approximation is made to calculate the

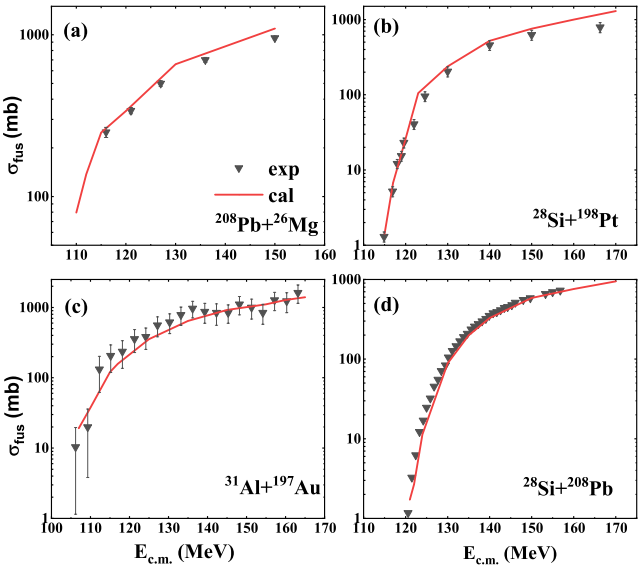

Fig. 2 Comparison between the fusion cross sections calculated by the IQMD model in ^{208}Pb+^{26}Mg, ^{28}Si+^{208}Pb, ^{31}Al+^{197}Au, and ^{28}Si+^{198}Pt reactions and the corresponding experimental results [56–59]. The corresponding data are denoted by lines and inverted solid triangles, respectively

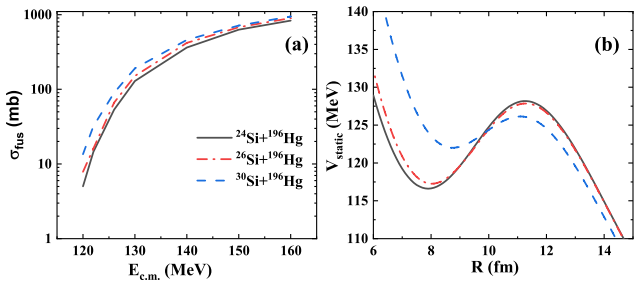

Fig. 3 (Color online) The fusion cross sections (**a**) and static interaction potentials (**b**) in the reactions ^{24,26,30}Si+^{196}Hg, represented by solid, dash-dotted, and dashed lines, respectively

static interaction potential, which means that the densities of both the projectile and target remain unchanged. Because the projectile and target are oblate, the directional effect on the static barriers should be considered. Hence, a random rotation for the projectile and target was made at the initial time for each event; then, we averaged the static barriers over a number of events. The isospin effect on the fusion cross section can be roughly understood by analyzing the static barrier. The static fusion barrier in the reaction with ^{30}Si beam exhibited the lowest height and narrowest width, leading to the greatest likelihood of overcoming the barrier.

The fusion process exhibits different characteristics for the various impact parameters. In Fig. 4, the fusion probability with respect to the impact parameter in reactions ^{24,26,30}Si+^{196}Hg at different incident energies is presented.

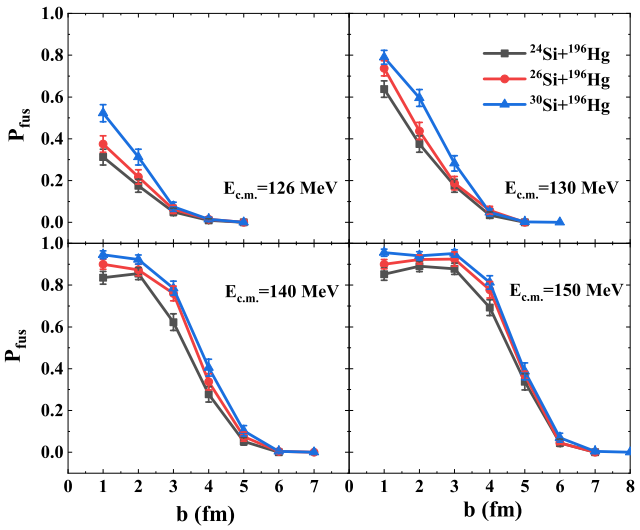

Fig. 4 (Color online) The fusion probability in the reactions ^{24,26,30}Si+^{196}Hg at different incident energies as a function of impact parameters, denoted by squares, circles, and triangles, respectively

It is evident that the fusion probability decreases as the impact parameters increase. This trend primarily arises from the influence of the rotational energy, which increases progressively with increasing impact parameters. Consequently, the reduction in the radial relative kinetic energy leads to a decrease in the fusion probability. In addition, the reaction mechanism transitions from the fusion reaction to the multinucleon transfer process and quasi-elastic scattering with increasing impact parameter; therefore, the competition among these mechanisms leads to a decrease in fusion probability. It can be observed that the neutron-rich system exhibits a higher fusion probability than a neutron-deficient system. This indicates that the fusion probability in neutron-rich systems is higher regardless of the impact parameters. It is worth noting that even at a sub-barrier energy of $E_{\text{c.m.}} = 126$ MeV, the fusion probability is nonnegligible.

The fusion reaction is a dynamical process involving a large number of nucleon transfers; thus, the impact of the dynamical interaction potential should be considered. The dynamical interaction potential between two nuclei depends not only on the reaction system but also on the incident energy. In Fig. 5, the dynamical and static interaction potential in ^{24,26,30}Si+^{196}Hg reactions at different energies is shown. It can be found that the dynamical barrier decreases with decreasing incident energy. That is attributed to the fact that the interaction time between the two nuclei is longer at a lower incident energy, giving the nucleons more time to adjust their density distribution to reach the lowest potential state. This indicates that sub-barrier fusion involves a process of passing over the barrier rather than the tunneling effect. Similar to the static barrier, the neutron-rich system exhibits a lower dynamical barrier. As the incident energy increases, the dynamical barriers first approach the static barriers and then surpass them. The same phenomenon has been described in Ref. [60]. Compared to static barriers, dynamical barriers appear at longer distances.

Owing to the effect of the nuclear structure quantities, such as the deformation of nuclei, the dynamical barrier and its moment are distributed within a certain range. Figure 6(a) shows the moment when the dynamical barrier appears in ^{30}Si+^{196}Hg reaction at different energies. The distributions of the dynamical barrier and its moment are shown in Fig. 6(c) and (b), respectively. It can be seen that at the sub-barrier incident energies of $E_{\text{c.m.}} = 125$ and 130 MeV, most events are concentrated around $t = 290$ fm/c. However, some events exhibit a longer duration and disperse at approximately 375 fm/c at a lower energy. The dispersion phenomenon gradually disappears as the incident energy increases.

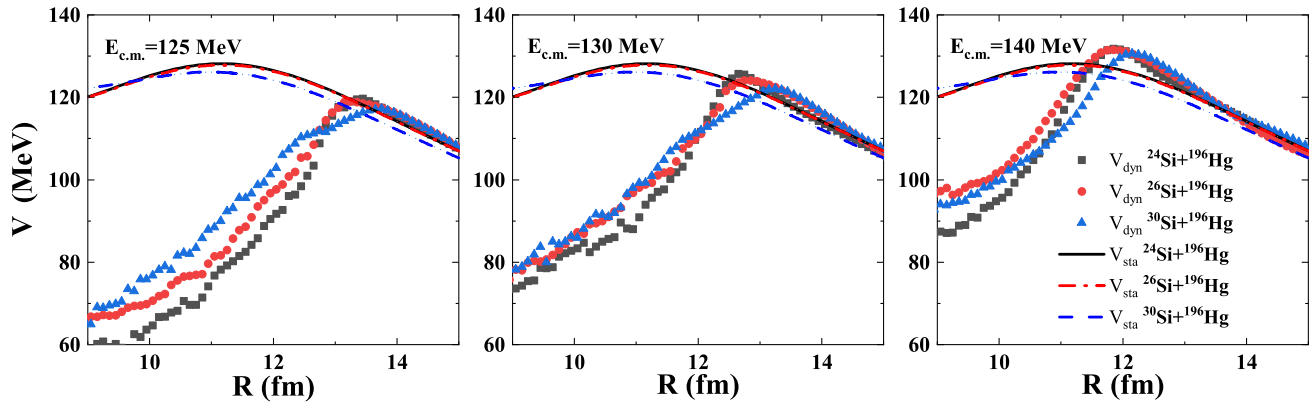

Fig. 5 (Color online) The dynamical interaction potentials in ^{24,26,30}Si+^{196}Hg reactions are represented by squares, circles, and triangles, respectively. The static interaction potentials in ^{24,26,30}Si+^{196}Hg reactions are represented by solid, dash-dotted, and dashed lines, respectively

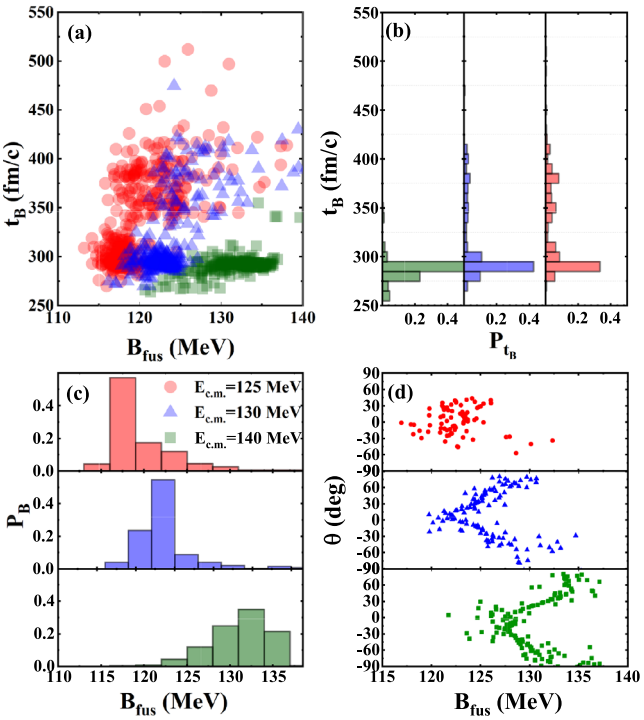

Fig. 6 (Color online) **a** The scatter diagram of the moment of the dynamical barrier in ^{30}Si+^{196}Hg reaction at $E_{c.m.}$ = 125, 130, and 140 MeV is represented by circles, triangles, and squares, respectively. **b** The distribution of the moment of the dynamical barrier and the incident energy decreases from the left to the right subfigure. **c** The distribution of dynamical barrier and the incident energy decreases from the top to the bottom subfigure. **d** The distribution of barrier heights at various collision orientations of the target

This indicates that the fusion process takes a longer time to exchange nucleons between the projectile and target in some events. As the incident energy increases, the barrier distribution gradually shifts to a higher-barrier region. Hence, the dynamical barrier is larger at higher incident energies, as shown in Fig. 5. The effect of the barrier height on the orientation of the target is shown in Fig. 6(d). θ denotes the angle between the symmetry axis of the target and collision direction. It can be found that the fusion barrier is significantly higher when the target is in the belly orientation, which is the same as described in Ref. [61]. At $E_{c.m.}$ = 125 MeV, the fusion barriers are predominantly distributed around the range from −45° to 45°. With increasing incident energy, fusion reaction events can also occur in the belly orientation because the incident energy is sufficiently high to overcome the Coulomb barrier in that orientation.

Neck formation is advantageous for nucleon transfer and fusion. In the IQMD model, the neck region is defined as a cylinder whose axis is along the line connecting the centroids of the two nuclei with a length of 4 fm, and whose lowest density at the center of mass is at least 0.02/fm^3. The width of the cylinder is defined as the neck radius. In Fig. 7(a), the time evolution of the *N*/*Z* ratio in the reactions ^{24,26,30}Si+^{196}Hg at $E_{c.m.}$ = 140 MeV is shown. It can be observed that the *N*/*Z* ratio grows rapidly to a peak at approximately t = 300 fm/c, then decreases, and eventually approaches the *N*/*Z* ratio of the compound nucleus. The increase in *N*/*Z* at the early stage is because the long-range Coulomb repulsion causes protons to move away from the neck region. As the projectile and target further overlap with time, more protons are transferred into the neck

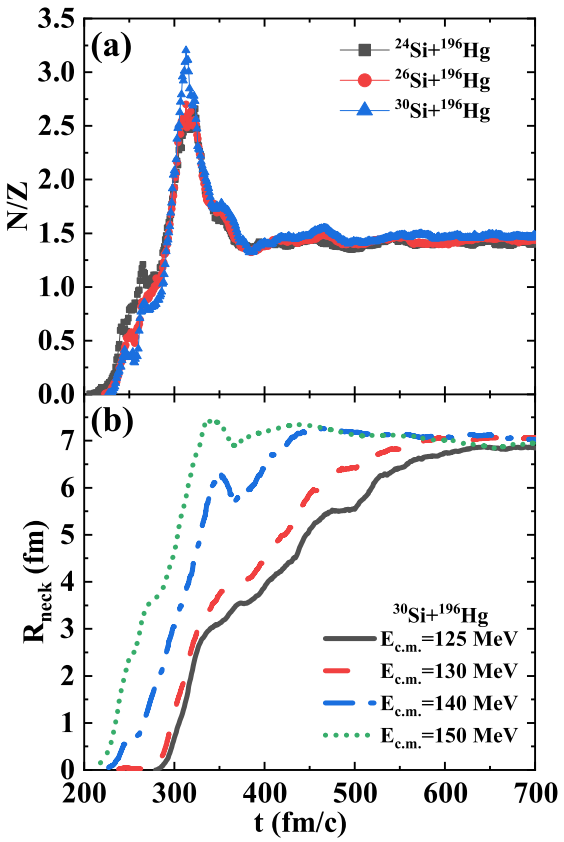

Fig. 7 (Color online) **a** The time evolution of the *N*/*Z* ratio in the neck region in the reactions ^{24,26,30}Si+^{196}Hg, denoted by squares, circles, and triangles, respectively. **b** The time evolution of the neck radius in the reactions ^{30}Si+^{196}Hg at $E_{c.m.}$ = 125, 130, 140, and 150 MeV, denoted by solid, dashed, dash-dotted, and dotted lines, respectively

region, leading to a decrease in *N*/*Z* ratio. It can be found that the peak value of *N*/*Z* ratio is the largest in the reaction ^{30}Si+^{196}Hg, indicating that neutrons flow to the neck more easily in neutron-rich system.

To investigate the growth of neck size, the time evolution of the neck radius at different energies is shown in Fig. 7(b): It can be noticed that the neck appears earlier and grows faster at a higher incident energy. In contrast, it takes longer to reach the size of the compound nucleus at a lower energy. This is because more time is required to exchange nucleons and adjust the density distribution to decrease the dynamical barrier.

To compare proton transfer with neutron transfer for analyzing the *N*/*Z* ratio in the neck region, Fig. 8 shows the neutron and proton density distribution in ^{30}Si+^{196}Hg reaction at $E_{\text{c.m.}} = 140$ MeV for different impact parameters. It can be seen that the neck region is larger at $b = 0$ compared to that at higher impact parameters. As the impact parameter increases, the neck gradually disappears, indicating that the neck grows faster at lower impact parameters. Compared to the proton density distribution, the neck region for neutrons is larger, meaning that neutrons transfer more quickly than protons during the evolution process, leading to a high *N*/*Z* ratio in the neck.

To study the motion trends of nucleon during its transfer processes, the single-particle potential in ^{30}Si+^{196}Hg reaction at $E_{\text{c.m.}} = 140$ MeV under different impact parameters is shown in Fig. 9. At $b = 0$, we find that the single-particle potential barrier decreases with time and consequently disappears at $t = 350$ fm/c, which indicates that the nucleon transfer between the projectile and target is easier at a lower impact parameter. However, at $b = 5$ fm, the barrier exists all the time, decreases first, and gradually increases as the two nuclei separate; thus, the nucleon transfer becomes obstructed. In addition, the single-particle potential barrier is higher at larger impact parameters at the same time.

The density distribution can be used to analyze the reaction mechanism, which is affected by the single-particle potential. The time evolution of density distribution in ^{30}Si+^{196}Hg reaction is shown in Fig. 10. One can notice that the neck region is smaller with a larger impact parameter at the same time. In addition, the neck grows slower under larger impact parameters, and the neck area decreases and tends to disappear at $b = 5$ fm, indicating that the harder it is for nucleons to transfer, the smaller the neck area is. Comparing the density distribution and single-particle potential, the disappearance of the single-particle potential barrier can promote the fusion event, and the increase in the

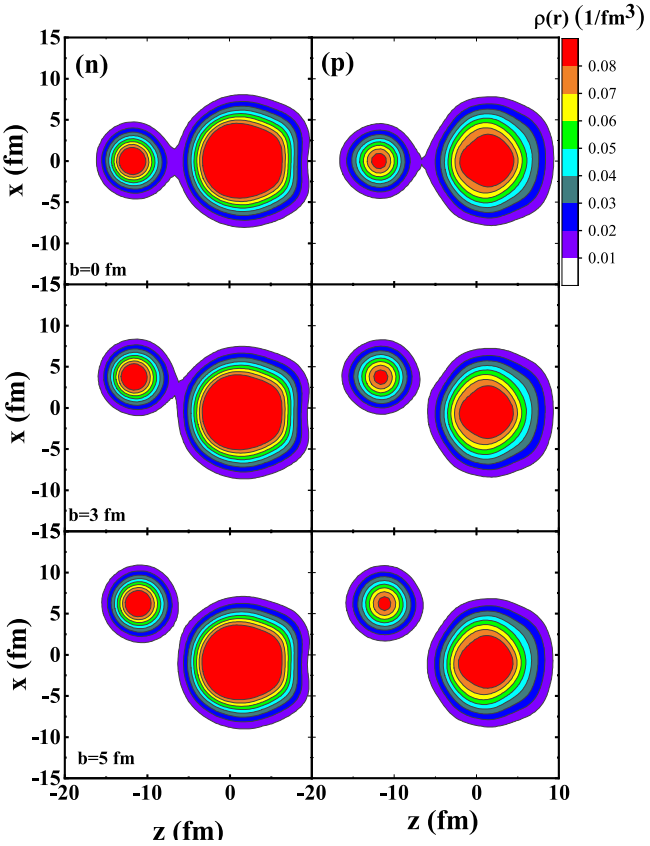

Fig. 8 (Color online) Neutron (left side) and proton (right side) density distributions at $b = 0$, 3, and 5 fm, $t = 250$ fm/c and $E_{\text{c.m.}} = 140$ MeV in ^{30}Si+^{196}Hg reaction

single-particle potential barrier can prevent nucleon flow and separate the two fragments.

4 Conclusion

The fusion mechanism to synthesize neutron-deficient Pu isotopes is investigated in the reactions ^{24,26,30}Si+^{196}Hg by the IQMD model. The calculated fusion cross sections agreed reasonably well with the available experimental data. The fusion cross sections in the reaction with more neutron-rich beams are larger owing to the lower static and dynamical barriers. The fusion probability decreases with an increasing impact parameter and is larger in the reaction with a more neutron-rich beam.

The dynamical barrier is reduced with decreasing incident energy, which explains the fusion enhancement at the sub-barrier energy. As the incident energy increases, the dynamical barriers first approach the static barriers and then surpass them, and the dynamical barrier distribution gradually shifts to a higher-barrier region. The time distribution of the appearance of dynamical barriers is wider at a lower incident energy, indicating that the fusion process takes a longer time to exchange nucleons. The fusion barrier was significantly higher when the target was oriented belly.

The neck dynamics of fusion reactions were studied. The peak value of *N*/*Z* ratio in the neck region is the highest in the reaction ^{30}Si+^{196}Hg, indirectly leading to a lowest dynamical barrier. The growth of the neck radius is slower at a lower incident energy. Comparing with the proton density distribution, the neck region for neutron is larger, meaning that neutrons transfer more quickly than protons, leading to a high *N*/*Z* ratio in the neck.

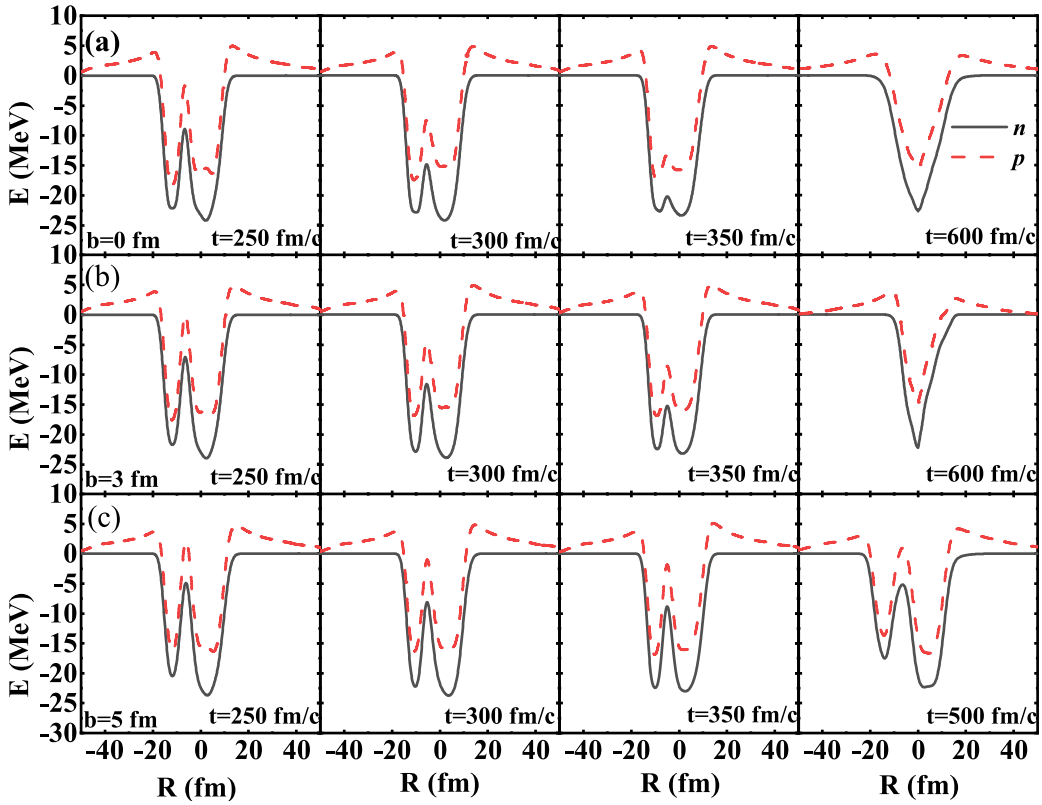

Fig. 9 (Color online) The time evolution of neutron and proton single-particle potentials in ^{30}Si+^{196}Hg reaction at different impact parameters, represented by the solid and dashed lines, respectively

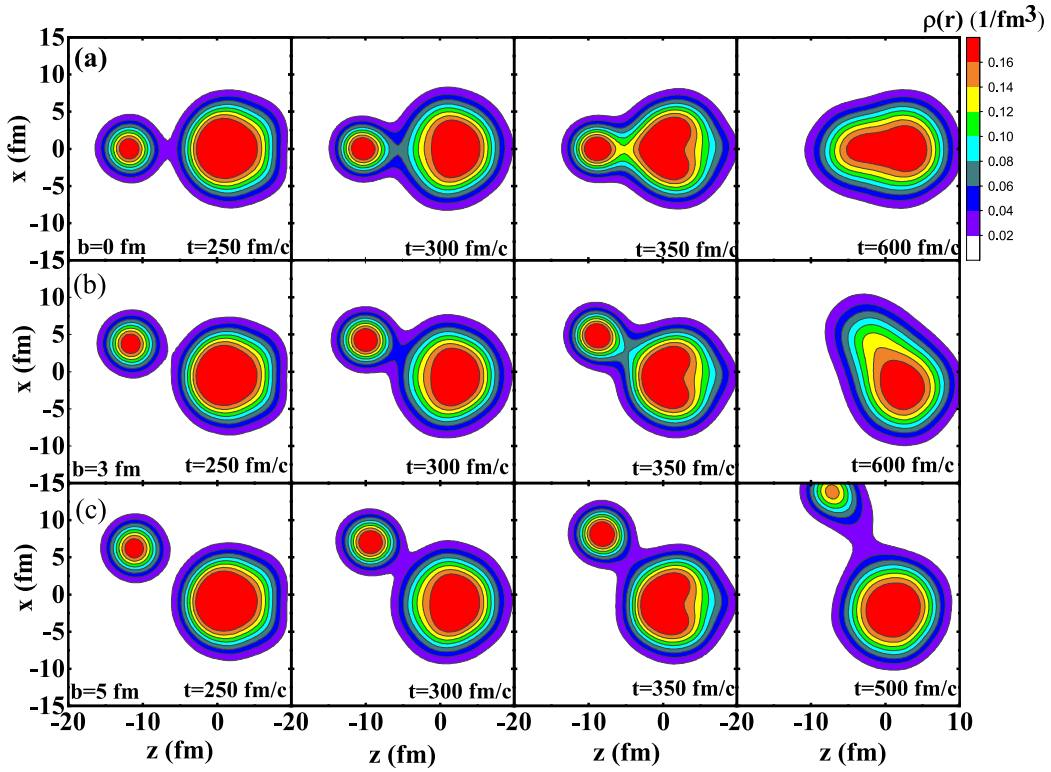

Fig. 10 (Color online) The time evolution of density distribution at $b = 0$ (**a**), $b = 3$ fm (**b**), and $b = 5$ fm (**c**) at $E_{\text{c.m.}} = 140$ MeV

The single-particle fusion barrier decreases with time and finally disappears at a lower impact parameter; therefore, the nucleon transfer between the projectile and target is easier. The disappearance of single-particle potential barrier can promote the fusion events.

Author contributions All authors contributed to the study conception and design. Material preparation, data collection, and analysis were performed by Zi-Long Wang, Xiao-Ye Zhang, Gen Zhang, and Feng-Shou Zhang. The first draft of the manuscript was written by Zi-Long Wang, and all authors commented on previous versions of the manuscript. All authors read and approved the final manuscript.

Declarations

Conflict of interest Feng-Shou Zhang is an editorial board member for Nuclear Science and Techniques and was not involved in the editorial review, or the decision to publish this article. All authors declare that there are no conflict of interest.

References

1. P. Guo, X.J. Cao, K.M. Chen et al., Nuclear mass table in deformed relativistic Hartree–Bogoliubov theory in continuum, II: even-Z nuclei. At. Data Nucl. Data Tables **158**, 101661 (2024). https://doi.org/10.1016/j.adt.2024.101661
2. C. Fry, M. Thoennessen, Discovery of the thallium, lead, bismuth, and polonium isotopes. At. Data Nucl. Data Tables **99**, 365 (2013). https://doi.org/10.1016/j.adt.2012.01.005
3. C. Fry, M. Thoennessen, Discovery of the astatine, radon, francium, and radium isotopes. At. Data Nucl. Data Tables **99**, 497–519 (2013). https://doi.org/10.1016/j.adt.2012.05.003
4. K. Satou, H. Ikezoe, S. Mitsuoka et al., Effect of shell structure in the fusion reactions ^{82}Se+^{134}Ba and ^{82}Se+^{138}Ba. Phys. Rev. C **65**, 054602 (2002). https://doi.org/10.1103/PhysRevC.65.054602
5. N. Wang, X. Wu, Z. Li et al., Applications of Skyrme energy-density functional to fusion reactions for synthesis of superheavy nuclei. Phys. Rev. C **74**, 044604 (2006). https://doi.org/10.1103/PhysRevC.74.044604
6. Z.Q. Feng, G.M. Jin, Fusion dynamics of symmetric systems near barrier energies. Phys. Rev. C **80**, 037601 (2009). https://doi.org/10.1103/PhysRevC.80.037601
7. B.M. Kayumov, O.K. Ganiev, A.K. Nasirov et al., Analysis of the fusion mechanism in the synthesis of superheavy element 119 via the ^{54}Cr+ ^{243}Am reaction. Phys. Rev. C **105**, 014618 (2022). https://doi.org/10.1103/PhysRevC.105.014618
8. A.N. Andreyev, M. Huyse, P. Van Duppen, Colloquium: beta-delayed fission of atomic nuclei. Rev. Mod. Phys. **85**, 1541–1559 (2013). https://doi.org/10.1103/RevModPhys.85.1541
9. M.V. Zhukov, I.J. Thompson, Existence of proton halos near the drip line. Phys. Rev. C **52**, 3505–3508 (1995). https://doi.org/10.1103/PhysRevC.52.3505
10. J. Elseviers, A.N. Andreyev, M. Huyse et al., β-delayed fission of ^{180}Tl. Phys. Rev. C **88**, 044321 (2013). https://doi.org/10.1103/PhysRevC.88.044321

11. A.N. Andreyev, S. Antalic, D. Ackermann et al., β-delayed fission of ^{192,194}At. Phys. Rev. C **87**, 014317 (2013). https://doi.org/10.1103/PhysRevC.87.014317
12. S.M. Wang, W. Nazarewicz, Puzzling two-proton decay of ^{67}Kr. Phys. Rev. Lett. **120**, 212502 (2018). https://doi.org/10.1103/PhysRevLett.120.212502
13. K.P. Santhosh, C. Nithya, Theoretical studies on the modes of decay of superheavy nuclei. Phys. Rev. C **94**, 054621 (2016). https://doi.org/10.1103/PhysRevC.94.054621
14. J.W. Kennedy, G.T. Seaborg, E. Segrè, Properties of 94(239). Phys. Rev. **70**, 555–556 (1946). https://doi.org/10.1103/PhysRev.70.555
15. R.A. James, A.E. Florin, H.H. Hopkins, A. Ghiorso, The Transuranium Elements: Research Papers, Paper 22.8, in: National Nuclear Energy Series IV, vol. 14b, McGraw-Hill, New York, p. 1604 (1949)
16. J.W. Kennedy, M.L. Perlman, E. Segre, A.C. Wahl, The Transuranium Elements: Research Papers, Paper 1.9, in: National Nuclear Energy Series IV, vol. 14b, McGraw-Hill, New York, p. 79 (1949)
17. G.T. Seaborg, R.A. James, L.O. Morgan, The Transuranium Elements: Research Papers, Paper 22.1, in: National Nuclear Energy Series IV, vol. 14b, McGraw-Hill, New York, p. 1525 (1949)
18. E.K. Hyde, M.H. Studier, A. Ghiorso, The Transuranium Elements: Research Papers, Paper 22.15, in: National Nuclear Energy Series IV, vol. 14b, McGraw-Hill, New York, p. 1622 (1949)
19. T.D. Thomas, R. Vandenbosch, R.A. Glass et al., Decay properties of Pu^{235}, Pu^{237}, and a new isotope Pu^{233}. Phys. Rev. **106**, 1228–1232 (1957). https://doi.org/10.1103/PhysRev
20. U. Jäger, H. Münzel, G. Pfennig, The decay of the neutron deficient plutonium isotopes ^{232}Pu, ^{233}Pu and ^{234}Pu. Z. Phys. A **258**, 337–343 (1973). https://doi.org/10.1007/BF01392443
21. C.A. Laue, K.E. Gregorich, R. Sudowe et al., New plutonium isotope: ^{231}Pu. Phys. Rev. C **59**, 3086–3092 (1999). https://doi.org/10.1103/PhysRevC.59.3086
22. A.N. Andreyev, D.D. Bogdanov, V.I. Chepigin et al., The new nuclide ^{230}Pu. Z. Phys. A **337**, 231–232 (1990). https://doi.org/10.1007/BF01294297
23. A.N. Andreyev, D.D. Bogdanov, V.I. Chepigin et al., New nuclides ^{228,229}Pu. Z. Phys. A **347**, 225–226 (1994). https://doi.org/10.1007/BF01292381
24. H.B. Yang, Z.G. Gan, Z.Y. Zhang et al., α decay of the new isotope ^{227}Pu. Phys. Rev. C **110**, 044302 (2024). https://doi.org/10.1103/PhysRevC.110.044302
25. S.G. Thompson, K. Street, A. Ghiorso et al., The new isotope ^{242}Pu and additional information on other plutonium isotopes. Phys. Rev. **80**, 1108–1109 (1950). https://doi.org/10.1103/PhysRev.80.1108
26. J.C. Sullivan, G.L. Pyle, M.H. Studier et al., Properties of Plutonium-243. Phys. Rev. **83**, 1267–1268 (1951). https://doi.org/10.1103/PhysRev.83.1267
27. M.H. Studier, P.R. Fields, P.H. Sellers et al., Plutonium-244 from pile-irradiated plutonium. Phys. Rev. **93**, 1433–1433 (1954). https://doi.org/10.1103/PhysRev.93.1433
28. C.I. Browne, D.C. Hoffman, W.T. Crane et al., The decay chain Pu^{245} Am^{245} Cm^{245}. J. Inorg. Nucl. Chem. **1**, 254–261 (1955). https://doi.org/10.1016/0022-1902(55)80030-9
29. Y.S. Popov, P.A. Privalova, G.A. Timofeev et al., Identification of ^{246}Pu, ^{247}Pu, ^{246m}Am, and ^{247}Am and determination of their half-lives. Sov. Radiochem. **25**, 4 (1984)
30. D. Engelkemeir, P.R. Fields, S. Fried et al., The new isotopes Pu^{246} and Am^{246}. J. Inorg. Nucl. Chem. **1**, 345–351 (1955). https://doi.org/10.1016/0022-1902(55)80044-9
31. S.A. Kalandarov, G.G. Adamian, N.V. Antonenko et al., Role of the entrance channel in the production of complex fragments in fusion-fission and quasifission reactions in the framework of the dinuclear system model. Phys. Rev. C **84**, 064601 (2011). https://doi.org/10.1103/PhysRevC.84.064601
32. J. Li, C. Li, G. Zhang et al., Theoretical study on production of unknown neutron-deficient $^{280\text{-}283}$Fl and neutron-rich $^{290\text{-}292}$Fl isotopes by fusion reactions. Phys. Rev. C **98**, 014626 (2018). https://doi.org/10.1103/PhysRevC.98.014626
33. M.H. Zhang, Y.H. Zhang, Y. Zou et al., Possibilities for the synthesis of superheavy element Z = 121 in fusion reactions. Nucl. Sci. Tech. **35**, 95 (2024). https://doi.org/10.1007/s41365-024-01452-y
34. P.H. Chen, H. Wu, Z.X. Yang et al., Prediction of synthesis cross sections of new moscovium isotopes in fusion-evaporation reactions. Nucl. Sci. Tech. **34**, 7 (2023). https://doi.org/10.1007/s41365-022-01157-0
35. C. Li, P.W. Wen, J. Li et al., Production of heavy neutron-rich nuclei with radioactive beams in multinucleon transfer reactions. Nucl. Sci. Tech. **28**, 110 (2017). https://doi.org/10.1007/s41365-017-0266-z
36. L. Zhu, J. Su, Unified description of fusion and multinucleon transfer processes within the dinuclear system model. Phys. Rev. C **104**, 044606 (2021). https://doi.org/10.1103/PhysRevC.104.044606
37. K. Mahboub, A. Zerarka, V.G. Foester, Fusion of heavy ions by means of the Langevin equation. Phys. Rev. C **71**, 064609 (2005). https://doi.org/10.1103/PhysRevC.71.064609
38. K. Sekizawa, K. Hagino, Time-dependent Hartree-Fock plus Langevin approach for hot fusion reactions to synthesize the $Z = 120$ superheavy element. Phys. Rev. C **99**, 051602 (2019). https://doi.org/10.1103/PhysRevC.99.051602
39. S. Amano, Y. Aritomo, M. Ohta, Dynamical mechanism of fusion hindrance in heavy ion collisions. Phys. Rev. C **108**, 014612 (2023). https://doi.org/10.1103/PhysRevC.108.014612
40. C. Shen, G. Kosenko, Y. Abe, Two-step model of fusion for the synthesis of superheavy elements. Phys. Rev. C **66**, 061602 (2002). https://doi.org/10.1103/PhysRevC.66.061602
41. W.J. Świątecki, K. Siwek-Wilczyńska, J. Wilczyński, Fusion by diffusion. II. Synthesis of transfermium elements in cold fusion reactions. Phys. Rev. C **71**, 014602 (2005). https://doi.org/10.1103/PhysRevC.71.014602
42. Z.H. Liu, J.D. Bao, Cold fusion reaction of ^{58}Fe + ^{208}Pb analyzed by a generalized model of fusion by diffusion. Phys. Rev. C **85**, 057603 (2012). https://doi.org/10.1103/PhysRevC.85.057603
43. L. Zhu, W.J. Xie, F.S. Zhang, Production cross sections of superheavy elements $Z = 119$ and 120 in hot fusion reactions. Phys. Rev. C **89**, 024615 (2014). https://doi.org/10.1103/PhysRevC.89.024615
44. V. Zagrebaev, W. Greiner, Synthesis of superheavy nuclei: a search for new production reactions. Phys. Rev. C **78**, 034610 (2008). https://doi.org/10.1103/PhysRevC.78.034610
45. S. Chopra, P.O. Hess, M.K. Sharma, Conspicuous role of the neck-length parameter for future superheavy element discoveries. Phys. Rev. C **108**, L021601 (2023). https://doi.org/10.1103/PhysRevC.108.L021601
46. S. Chopra, P.O. Hess, Predicted cross sections for the synthesis of $Z = 120$ fusion via ^{54}Cr+^{248}Cm and ^{50}Ti+^{249}Cf target-projectile combinations. Phys. Rev. C **110**, 014615 (2024). https://doi.org/10.1103/PhysRevC.110.014615
47. A.S. Umar, V.E. Oberacker, Time dependent Hartree-Fock fusion calculations for spherical, deformed systems. Phys. Rev. C **74**, 024606 (2006). https://doi.org/10.1103/PhysRevC.74.024606
48. X. Sun, L. Guo, Microscopic study of the hot-fusion reaction ^{48}Ca+^{238}U with the constraints from time-dependent Hartree-Fock theory. Phys. Rev. C **107**, 064609 (2023). https://doi.org/10.1103/PhysRevC.107.064609
49. C. Simenel, A.S. Umar, Heavy-ion collisions and fission dynamics with the time-dependent Hartree-Fock theory and its extensions.

Prog. Part. Nucl. Phys. **103**, 19–66 (2018). https://doi.org/10.1016/j.ppnp.2018.07.002
50. F.S. Zhang, L.W. Chen, Z.Y. Ming et al., Isospin dependence of nuclear multifragmentation in ^{112}Sn+^{112}Sn and ^{124}Sn+^{124}Sn collisions at 40 MeV/nucleon. Phys. Rev. C **60**, 064604 (1999). https://doi.org/10.1103/PhysRevC.60.064604
51. N. Wang, K. Zhao, Z.X. Li, Systematic study of ^{16}O induced fusion with the improved quantum molecular dynamics model. Phys. Rev. C **90**, 054610 (2014). https://doi.org/10.1103/PhysRevC.90.054610
52. D. Vautherin, D.M. Brink, Hartree-Fock calculations with Skyrme's interaction. I. Spherical Nuclei. Phys. Rev. C **5**, 626–647 (1972). https://doi.org/10.1103/PhysRevC.5.626
53. N. Wang, Z.X. Li, X.Z. Wu et al., Search for possible way of producing super-heavy elements: Dynamic study on damped reactions of ^{244}Pu+^{244}Pu, ^{238}U+^{238}U and ^{197}Au+^{197}Au. Mod. Phys. Lett. A **20**, 2619–2627 (2005). https://doi.org/10.1142/S0217732305018232
54. M. Papa, T. Maruyama, A. Bonasera et al., Constrained molecular dynamics approach to fermionic systems. Phys. Rev. C **64**, 024612 (2001). https://doi.org/10.1103/PhysRevC.64.024612
55. K. Chen, Z. Fraenkel, G. Friedlander et al., VEGAS: a Monte carlo simulation of intranuclear cascades. Phys. Rev. **166**, 949–967 (1968). https://doi.org/10.1103/PhysRev.166.949
56. R. Bock, Y.T. Chu, M. Dakowski et al., Dynamics of the fusion process. Nucl. Phys. A **388**, 334–380 (1982). https://doi.org/10.1016/0375-9474(82)90420-1
57. D.J. Hinde, C.R. Morton, M. Dasgupta et al., Competition between fusion-fission and quasi-fission in the reaction ^{28}Si+^{208}Pb. Nucl. Phys. A **592**, 271–289 (1995). https://doi.org/10.1016/0375-9474(95)00306-L
58. K. Nishio, H. Ikezoe, S. Mitsuoka et al., Fusion of deformed nuclei in the reactions of ^{76}Ge+^{150}Nd and ^{28}Si+^{198}Pt at the Coulomb barrier region. Phys. Rev. C **62**, 014602 (2000). https://doi.org/10.1103/PhysRevC.62.014602
59. Y.X. Watanabe, A. Yoshida, T. Fukuda et al., Measurement of fusion excitation functions of ^{27,29,31}Al+^{197}Au. Eur. Phys. J. A **10**, 373–379 (2001). https://doi.org/10.1007/s100500170102
60. L. Zhu, J. Su, W.J. Xie et al., Study of the dynamical potential barriers in heavy ion collisions. Nucl. Phys. A **915**, 90–105 (2013). https://doi.org/10.1016/j.nuclphysa.2013.07.003
61. Y.J. Feng, H.Z. Liu, Y.G. Huang et al., Microscopic study of deformation and orientation effects in heavy-ion reactions above the Coulomb barrier using the Boltzmann-Uehling-Uhlenbeck model. Phys. Rev. C **109**, 054604 (2024). https://doi.org/10.1103/PhysRevC.109.054604